



# On the Correlation between Near-Field Scan Immunity and Radiated Immunity at Printed Circuit Board Level – Part II

Alexandre Boyer, Nicolas Nolhier, Fabrice Caignet, Sonia Ben Dhia

## ► To cite this version:

Alexandre Boyer, Nicolas Nolhier, Fabrice Caignet, Sonia Ben Dhia. On the Correlation between Near-Field Scan Immunity and Radiated Immunity at Printed Circuit Board Level – Part II. *IEEE Transactions on Electromagnetic Compatibility*, 2022, 64 (5), pp.1493 - 1505. 10.1109/TEMC.2022.3172601 . hal-03681022

HAL Id: hal-03681022

<https://laas.hal.science/hal-03681022>

Submitted on 30 May 2022

**HAL** is a multi-disciplinary open access archive for the deposit and dissemination of scientific research documents, whether they are published or not. The documents may come from teaching and research institutions in France or abroad, or from public or private research centers.

L'archive ouverte pluridisciplinaire **HAL**, est destinée au dépôt et à la diffusion de documents scientifiques de niveau recherche, publiés ou non, émanant des établissements d'enseignement et de recherche français ou étrangers, des laboratoires publics ou privés.

# On the Correlation between Near-Field Scan Immunity and Radiated Immunity at Printed Circuit Board Level – Part II

A. Boyer, N. Nolhier, F. Caignet, S. Ben Dhia

**Abstract**—The work presented in this two-part paper focuses on a prediction method of the radiated susceptibility of integrated circuit and printed circuit board from near-field scan injection, in order to anticipate risks of non-compliance due to design weakness. In Part I, a worst-case estimator of the far-field induced voltage on a PCB trace was proposed. Based on it, an estimator of the radiated susceptibility of a printed-circuit board based on near-field scan results is derived and validated through two validation case studies.

**Index Terms**— Near-field scan, radiated susceptibility, near-field probe

## I. INTRODUCTION

NEAR-field scan immunity (NFSI) [1] is a powerful diagnostic tool that reveals coupling areas at the integrated circuit (IC) and printed circuit board (PCB) levels, and that helps electromagnetic compatibility (EMC) experts and designers to identify the root-cause of failures that may trigger during radiated susceptibility (RS) tests. In part I of this two-part paper, several examples of NFSI applications were presented [2]-[8]. This research work aims at providing post-processing methods of NFSI results in order to assess RS risks at the IC and PCB levels. Part I reviewed several attempts to relate the RS level to NFSI results [9]-[10]. However, these attempts require preliminary RS test results or the extraction of phase information during NFSI, which make them unpractical.

The first part of this paper clarified the link between far-field (FF) and near-field (NF) coupling on a microstrip line terminated by linear loads. We demonstrated that the precise FF-induced voltage cannot be determined from NFSI results, but a worst-case estimator of the FF-induced voltage can be derived. This may be sufficient for RS risk assessment. The proposed approach relies on accurate knowledge of the field produced by the NF injection probes. It can be obtained by a proper calibration process, which was described and validated in Part I. However, the proposed approach is not perfectly adapted to RS testing, which aims at determining the amount of radiated disturbance that leads to the failure of an electronic device. Moreover, practical electronic systems embed non-

linear functions and radiated disturbance simultaneously illuminates several traces of PCB. The effect of this simultaneous coupling cannot be predicted with precision from NFSI results because of local coupling with the NF probe, as pointed out in [11].

The second part of this paper addresses these issues and proposes two practical studies to evaluate the impact of these limitations on RS risk assessment. In Section II, the NF-based FF coupling estimator is revised to derive an estimation of the RS level from NFSI results. The underlying assumptions are emphasized. In Section III, the estimator is amended to respond to a practical issue in NFSI testing: determining the maximum excitation power to ensure that the NFSI test is representative of RS test limits. Section IV describes the two case studies (first at the IC level, then at the PCB level) dedicated to validation of the proposed estimator. Finally, results are presented in Section V, where RS measurements in gigahertz transverse electromagnetic (GTEM) cells are compared with the proposed NFSI-based estimator.

## II. ESTIMATION OF RADIATED SUSCEPTIBILITY FROM NEAR-FIELD SCAN INJECTION

### A. Theoretical Formulation

Let us consider a straight microstrip line of length  $L$  terminated by two loads and one of them (Load 1) is an IC input whose susceptibility to radio frequency (RF) disturbance is investigated. The line is excited by harmonic radiated disturbances: either FF disturbance, i.e. plane wave illumination with random angles of incidence and polarization, or NF injection, i.e. an E or H-field probe placed in an arbitrary position above the line. The position of the problem is described in Fig. 1. The purpose is to estimate the RS level from NFSI results, i.e. to determine the minimum amplitude of the incoming plane wave that may induce a failure, here in Load 1. Certain assumptions are made about the nature of the termination Load 1. The impedance is assumed to be linear or quasi-linear, i.e. it does not depend on the induced voltage across the load. In practice, this assumption is valid for IC pins as long as internal electrostatic discharge (ESD) protections are not triggered. However, the internal function that relates the

This work was supported by the Nanoscan project (CNES No. 200111/00) sponsored by the French National Centre for Space Studies (CNES).

A. Boyer, N. Nolhier, F. Caignet and S. Ben-Dhia work at the LAAS, Univ. de Toulouse, INSA, Toulouse, France (e-mail: [alexandre.boyer@laas.fr](mailto:alexandre.boyer@laas.fr), [nolhier@laas.fr](mailto:nolhier@laas.fr), [fcaignet@laas.fr](mailto:fcaignet@laas.fr), [sonia.bendhia@insa-toulouse.fr](mailto:sonia.bendhia@insa-toulouse.fr)).

load behavior to the input RF voltage may be non-linear. A failure is triggered if the amplitude of the voltage across the load  $V_{LI}$  exceeds a limit  $V_{Fail}$ . This model supposes that the failure depends mainly on the RF voltage induced on only one trace. Due to local coupling of the NF injection, the effect of simultaneous radiated coupling on several traces cannot be reproduced during NFSI testing. The risk is overestimation or underestimation of the RS level from NFSI results, depending on how the different coupling contributions combine.

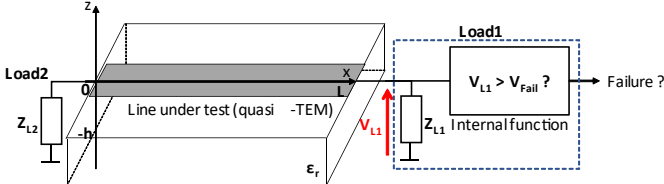


**Fig. 1.** Equivalent model of the illuminated line terminated by an integrated circuit input (Load 1)

In Part I of this paper, the estimator  $V_{L1}^{NF \rightarrow FF}$  of the worst-case FF-induced voltage based on NFSI results was derived (1). It provides an upper bound of the maximum induced voltage along the line terminal illuminated by a plane wave whose E-field amplitude is  $E_0$ , regardless of the plane wave incidence direction and polarization.  $V_{LE}^{NF max}$  and  $V_{LH}^{NF max}$  are the maximum induced voltage during E and H-field injection tests.  $E_{Z max}^{NF}$  and  $H_{Y max}^{NF}$  are the average E and H-fields produced by the E and H-field injection probe along the line. (2) defines a cut-off frequency between the low and high frequency regimes of the line illuminated by a plane wave. Below  $f_c$ , the line portion on which the incoming wave couples is electrically short, so all this line portion is illuminated in phase. Above  $f_c$ , this line portion becomes electrically long and the incoming wave is not in phase along it.

$$V_{L1}^{NF \rightarrow FF}(E_0) = \frac{2E_0 V_{LE}^{NF max}}{E_{Z max}^{NF} \epsilon_r \sqrt{1 + \left(\frac{f}{f_c} \frac{\epsilon_r}{\epsilon_{eff}}\right)^2}} + \frac{2E_0 V_{LH}^{NF max}}{\eta_0 H_{Y max}^{NF} \sqrt{1 + \left(\frac{f}{f_c}\right)^2}} \quad (1)$$

$$f_c = \frac{c_0}{2\pi L} \left( \sqrt{\epsilon_{eff}} - 1 \right) \left( 1 - \frac{\sqrt{\epsilon_{eff}}}{\epsilon_r} \right)^{-1} \quad (2)$$

In the case described in Fig 1, this estimator can be used to determine  $V_{LI}$  as the termination impedances are assumed to be linear. The relationship (3) between the worst-case FF-induced voltage  $V_{worst}^{FF}$  for the  $E_0$  field illumination and the estimator (1) can be written. Let us consider  $E_{min}^{FF}$  to be the minimum amplitude of the plane wave illumination that leads to a failure, i.e., in the worst-case coupling situation. When a failure arises, regardless of the type of radiated disturbance,  $V_{LI}$  is equal to  $V_{Fail}$ . If the failure is triggered during E and H-field injection, the terms  $V_{LE}^{NF max}$  and  $V_{LH}^{NF max}$  are equal to  $V_{Fail}$ . If the failure arises during the RS test in the worst-case coupling situation,  $V_{worst}^{FF}$  is also equal to  $V_{Fail}$ . Substituting  $V_{Fail}$  into (1) and (3) leads to (4), which gives the lower bound of  $E_{min}^{FF}$  according to the average E and H-field produced by the injection probes when a failure arises during NFSI measurements.

$$V_{worst}^{FF}(E_0) \leq V_{L1}^{NF \rightarrow FF}(E_0) \quad (3)$$

$$E_{min}^{FF} \geq \frac{1}{2} \left( \frac{1}{E_{Z max}^{NF} \epsilon_r \sqrt{1 + \left(\frac{f}{f_c} \frac{\epsilon_r}{\epsilon_{eff}}\right)^2}} + \frac{1}{\eta_0 H_{Y max}^{NF} \sqrt{1 + \left(\frac{f}{f_c}\right)^2}} \right)^{-1} \quad (4)$$

In this estimator of the RS of a PCB line to a plane wave illumination, the contributions of E and H-field couplings are clearly visible and can be compared. Let  $Z_N$  be the ratio given by (5), which is the normalized wave impedance. The practical interest of this ratio is that it points out the predominance of E or H-field coupling contributions to the induced failure during the RS test. If  $Z_N > 1$ , the contribution of H-field coupling dominates, while the E-field coupling contribution dominates if  $Z_N < 1$ .

$$Z_N = \frac{E_{Z max}^{NF}}{\eta_0 H_{Y max}^{NF}} \quad (5)$$

### B. Practical Implementation of the Estimation Method

Equations (1), (2) and (4) have been derived in the case of a straight line. In practical PCB traces or package interconnects, lines can be bended. They are composed of several portions with various directions on which different field components can couple. Thus, the E and H field components of the incoming disturbance couple on different line portions, whose lengths are not necessarily equal to the total length  $L$  of the line. The expressions of Section II.A can be extended to the case of a bended line if a new term is introduced: the coupling length  $L_C$ , which is the line portion on which a field component can couple. Except for a straight line, the coupling length may be different for each field component. For bended microstrip, it is especially true for H-field, which cannot couple along the entire line, but only on line portions that are not parallel to the H-field direction. The coupling length for one H-field component is equal to the total length of these portions.

Let suppose that E and H field components couple on different portions of the line under test. (1) can be rewritten to (6), where  $L_{CE}$  and  $L_{CH}$  are the coupling lengths associated to E and H-fields. The RS estimator (4) can be rewritten to (9).

$$V_{L1}^{NF \rightarrow FF}(E_0) = \frac{2E_0 V_{LE}^{NF max}}{E_{Z max}^{NF} \epsilon_r \sqrt{1 + \left(\frac{f}{f_{CE}} \frac{\epsilon_r}{\epsilon_{eff}}\right)^2}} + \frac{2E_0 V_{LH}^{NF max}}{\eta_0 H_{Y max}^{NF} \sqrt{1 + \left(\frac{f}{f_{CH}}\right)^2}} \quad (6)$$

$$f_{CE} = \frac{c_0}{2\pi L_{CE}} \left( \sqrt{\epsilon_{eff}} - 1 \right) \left( 1 - \frac{\sqrt{\epsilon_{eff}}}{\epsilon_r} \right)^{-1} \quad (7)$$

$$f_{CH} = \frac{c_0}{2\pi L_{CH}} \left( \sqrt{\epsilon_{eff}} - 1 \right) \left( 1 - \frac{\sqrt{\epsilon_{eff}}}{\epsilon_r} \right)^{-1} \quad (8)$$

$$E_{min}^{FF} \geq \frac{1}{2} \left( \frac{1}{E_{Z max}^{NF} \epsilon_r \sqrt{1 + \left(\frac{f}{f_{CE}} \frac{\epsilon_r}{\epsilon_{eff}}\right)^2}} + \frac{1}{\eta_0 H_{Y max}^{NF} \sqrt{1 + \left(\frac{f}{f_{CH}}\right)^2}} \right)^{-1} \quad (9)$$

A first practical issue is related to the identification of the coupling length for each field component. The practical implementation of (8) to estimate RS requires knowledge of the coupling length for each field component. They have a major influence on the estimated susceptibility level as it appears not only explicitly in (7) and (8), but also implicitly in (6) for the calculation of the average E or H-fields produced by the injection probe. The coupling lengths are not known from the outset and their extraction relies on the NFSI maps built from NFSI test results. Each point of the NFSI maps gives the required probe excitation to induce a failure when the probe is

placed at that point. Sensitive traces or IC package pins can be identified from its analysis, which focuses the RS estimation on these sensitive interconnects.

Once a sensitive trace has been detected from NFSI map analysis, the associated coupling length can be determined. As radiated disturbance couples only on interconnects routed on external board layers, identification of the sensitive traces and extraction of their lengths become obvious. This is the case of interconnects with well-known dimensions, e.g. traces routed on the external layers of PCB. However, the exact dimensions of interconnects are not necessarily available, for example for PCB with an encapsulation protective layer or IC package interconnects. In such a situation, the coupling length can be only extracted from the analysis of the NFSI maps. A sensitive interconnect appears as a local area where a small amount of probe excitation power is required to induce a failure. In this paper, if the coupling length is extracted from NFSI maps, it is defined as the length along which the excitation power remains at less than 6 dB of the minimum required power to induce a failure.

A second practical issue is due to the simultaneous coupling of radiated disturbance on several interconnects. This may happen in FF illumination of a board, but not during local NF injection. NFSI maps will show the different sensitive traces and their length can easily be identified. However, NFSI map analysis cannot provide information on how the contribution of the couplings on the different traces combine, since the NFSI map was built from results of local injection tests. Considering only the coupling on one trace could lead to overestimation of the actual RS, if these contributions counterbalance. Inversely, it could also lead to underestimation of the RS if these contributions add up. For EMC mitigation purposes, overestimation of the RS is better. This choice is made for estimation of the RS in the case studies presented in Section IV.

### III. ESTIMATING THE EXCITATION POWER OF THE NEAR-FIELD INJECTION PROBE

An important practical consideration of NFSI testing is defining the required excitation power of an NF injection probe to be representative of an RS test. The probe is assumed to have been calibrated according to the method described in Part I of this paper. In other words, this consists in determining the probe excitation power that generates either the same average E or H-field as a far-field illumination. It is necessary to dimension the power amplifier used for the NFSI test and make the link between NFSI test results and RS limits. Obviously, the NF injection cannot produce a plane wave whose coupling is distributed along the board under test. Moreover, the susceptibility of the DUT and the contributions of E and H-field couplings are still unknown before the tests. The estimation of the excitation to give to a probe must be done independently of the other probes. An upper bound of the maximum excitation power can be derived.

#### A. H-field Probe Excitation

Let us consider the tangential H-field injection probe. The maximum E-field amplitude used during the RS test is  $E_{max}^{FF}$ .

The FF-induced voltage  $V_{L1}^{FF}$  is upper bounded by (6), sum of E and H-field injection results which are unknown before the NFSI tests. The maximum excitation of the H-field probe is determined from (6) by considering only the effect of the H-field injection (the first term of the right side of (6)) and discarding the E-field injection (the second term of the right side of (6)). Thus, the excitation to provide to the H-field probe is calculated in such a way that it generates the same average H-field over the DUT than the plane wave with the maximum amplitude that would be used during the radiated susceptibility test. (6) is simplified to (10). When a failure arises, the induced voltage during H-field injection  $V_{LH}^{NF}$  is assumed to be equal to  $V_{L1}^{FF}$ , so the condition (11) about the average H-field produced by the probe along the line under test  $\overline{H_Y^{NF}}$  can be derived.

$$V_{L1}^{FF} \leq V_{L1}^{NF \rightarrow FF}(E_{max}^{FF}) = \frac{2E_{max}^{FF}V_{LH}^{NF}}{\eta_0 \overline{H_Y^{NF}} \sqrt{1 + \left(\frac{f}{f_{CH}}\right)^2}} \quad (10)$$

$$\overline{H_Y^{NF}} \leq \frac{2E_{max}^{FF}}{\eta_0 \sqrt{1 + \left(\frac{f}{f_{CH}}\right)^2}} \quad (11)$$

$\overline{H_Y^{NF}}$  can be determined from the magnetic dipole model used during probe calibration. Let us consider that the equivalent horizontal dipole is placed at a scan altitude  $R$  above the center of a long straight microstrip line oriented along x direction and routed at a height  $h$  above an infinitely large ground plane. In case of a straight line, the coupling length to H-field  $L_{CH}$  is equal to the total length of the line. In case of a bent line made of several straight portions, the coupling length is the length of the portions on which the probe disturbance can couple. For an actual H-field probe, the center of the equivalent magnetic dipole is placed at  $R+h_{inj}$  above the surface of the line, where the injection height  $h_{inj}$  was defined in Part I of this paper (Fig. 4) as the distance between the probe extremity and the center of the equivalent dipole. For small scan altitude and from the image theory, the tangential component  $H_Y$  on a point between the trace and the reference plane is given by (12). The magnetic moment  $m_H$  is related to the excitation power  $P_{excH}$  by the calibration parameters, as given by (13), where  $m_H^{ref}$  is the equivalent magnetic moment of the injection probe extracted during the calibration process, and  $P_{ref}$  the used excitation power. The average H-field  $\overline{H_Y}$  along the line section is given by integral (15), whose result is given by (16). The function  $f_{\bar{H}}$  gives  $\overline{H_Y}$  along  $L_{CH}$  with  $m_H$  equal to  $1 \text{ A}\cdot\text{m}^2$ . Substituting (16) into (11) leads to the maximum power  $P_{Hmax}$  required during H near-field injection (17) to produce the same average field along  $L_{CH}$  than an incoming plane wave of amplitude  $E_{max}^{FF}$ .

$$H_Y = \frac{\mu_0 \omega m_H}{4\pi \eta_0 k_0} \left( \frac{1}{((x-x_0)^2+R_1^2)^{\frac{3}{2}}} + \frac{1}{((x-x_0)^2+R_2^2)^{\frac{3}{2}}} \right) \quad (12)$$

$$m_H = m_H^{ref} \sqrt{\frac{P_{excH}}{P_{ref}}} \quad (13)$$

$$R_{1,2} = R + h_{inj} + h \pm z \quad (14)$$

$$\overline{H_Y} = \frac{1}{L_{CH}h} \int_{-L_{CH}/2}^{+L_{CH}/2} \int_0^h H_Y dz dx \quad (15)$$

Estimating  $P_{Hmax}$  requires the calibration parameters of the probe and setting various geometrical parameters. Some of them are known from the outset (e.g.,  $h$  and  $R$ ). However, the coupling length  $L_{CH}$  is known accurately only once the NFSI test is done. In practice, using (15) requires us to assume a likely value for  $L_{CH}$ , for example based on the dimensions of traces that are suspected to be sensitive.

$$\overline{H_Y} = m_H f_{\bar{H}} = \frac{m_H}{\pi h L_{CH}^2} \left( \frac{\sqrt{\left(\frac{L_{CH}}{2}\right)^2 + (R+h_{inj})^2}}{R+h_{inj}} - \frac{\sqrt{\left(\frac{L_{CH}}{2}\right)^2 + (R+h_{inj}+2h)^2}}{R+h_{inj}+2h} \right) \quad (16)$$

$$P_{Hmax} = \frac{P_{ref}}{1 + \left(\frac{f}{f_{CH}}\right)^2} \left( \frac{2E_{max}^{FF}}{\eta_0 m_H^{ref} f_{\bar{H}}} \right)^2 \quad (17)$$

(17) is based on the infinite large ground plane assumption, which may not be met with a practical finite size board. To evaluate the effect of the finite size of the board on the average H-field produced by the injection probe, 3D electromagnetic simulations made with FEKO software [12] are performed to compare the field produced by an elementary magnetic dipole placed above either a finite or infinite ground plane. The probe is placed above the middle of a square-shaped board, and the average tangential H-field is computed along the entire board.

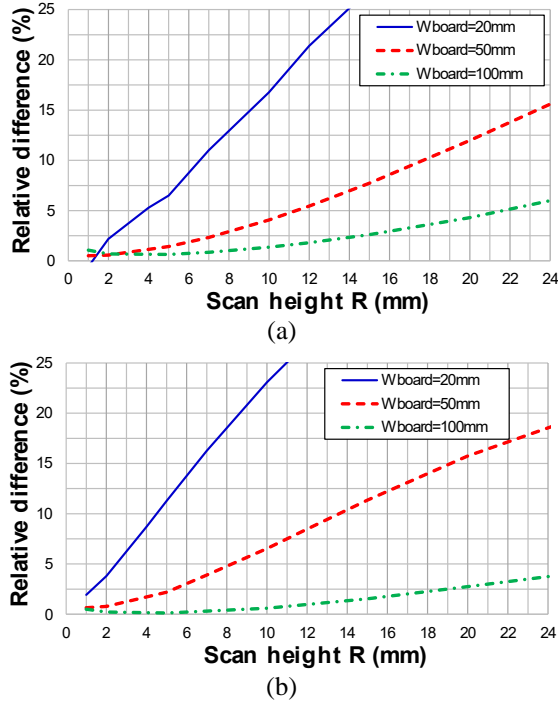


**Fig. 2.** Relative difference between the average field computed above a finite and an infinite ground plane: (a) Tangential H-field produced by a magnetic injection probe, (b) Vertical E-field produced by an electric injection probe

The relative difference between the H-field computed with the finite and infinite ground planes is plotted vs. the scan height  $R$  for three different board sizes  $W_{board}$ , as shown in Fig. 2-a. The result shows that the relative difference remains less than 5

\%, as long as the scanning height is smaller than nearly one fifth of the board width. For practical boards with dimensions larger than several tens of millimeters, the infinite ground plane assumption remains acceptable for a scan height less than several millimeters, which is typically used.

### B. E-field Probe Excitation

The same approach can be used to determine the maximum excitation power of the normal E-field probe. Similarly, the maximum excitation of the E-field probe is determined from (6) by considering only the effect of the E-field injection and discarding the H-field injection. Thus, the excitation to provide to the E-field probe is calculated in such a way that it generates the same average E-field over the DUT than the plane wave with the maximum amplitude that would be used during the radiated susceptibility test. (6) is simplified to (18) which provides an upper bound of the FF-induced voltage  $V_{L1}^{FF}$ . It leads to the condition (19) about the average E-field  $\overline{E}_Z^{NF}$  produced by the probe along the line under test can be derived.

$$V_{L1}^{FF} \leq f_{NF \rightarrow FF}(E_{max}^{FF}) = \frac{2E_{max}^{FF} V_{LE}^{NF}}{\overline{E}_Z^{NF} \epsilon_r \sqrt{1 + \left(\frac{f}{f_{CE}} \frac{\epsilon_r}{\epsilon_{eff}}\right)^2}} \quad (18)$$

$$\overline{E}_Z^{NF} \leq \frac{2E_{max}^{FF}}{\epsilon_r \sqrt{1 + \left(\frac{f}{f_{CE}} \frac{\epsilon_r}{\epsilon_{eff}}\right)^2}} \quad (19)$$

However, extracting the expression of  $\overline{E}_Z^{NF}$  is complex due to the multiple reflections created by the air-dielectric interface and the ground plane. The multiple partial image method [13] can be used to compute the E-field produced by the injection probe within the substrate. For more details, the reader can refer to Part I of this paper.

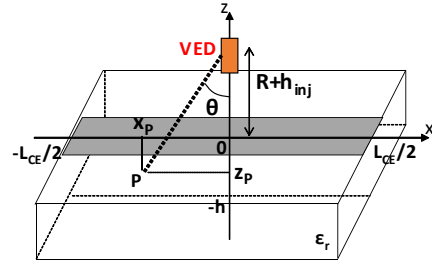


**Fig. 3.** Vertical electric dipole placed above a microstrip line

The normal E-field probe is modeled as a vertical electric dipole (VED). It is placed at scan altitude  $R$  above the center of a long microstrip line oriented along  $x$  direction and routed at a height  $h$  above an infinitely large ground plane, as illustrated in Fig 3. Initially, let us ignore the effect of the ground plane and the dielectric layer. Only the direct contribution of the VED is considered. For small scan altitude, the normal E-field component  $E_z$  is given by (20). The electric moment  $m_E$  is related to the excitation power  $P_{excE}$  by the calibration parameters (21), where  $m_E^{ref}$  is the equivalent magnetic moment of the injection probe extracted during the calibration process, and  $P_{ref}$  the used excitation power. The average normal E-field  $\overline{E}_Z$  along the line section is given by integral (22), whose result is given by (23). The function  $f_E^0$  gives

$\overline{E_Z}$  along the coupling length  $L_{CE}$  produced by the direct contribution of the dipole excited with  $m_E$  equal to 1 A·m.

$$\overline{E_Z} = \frac{m_E}{2\pi\omega\epsilon_0} \left( -\frac{3\cos^2\theta}{2} + \frac{1}{2r^3} \right) = \frac{m_E}{2\pi\omega\epsilon_0} \left( -\frac{3}{2} \frac{(z_p-R-h_{inj})^2}{(x_p^2+(z_p-R-h_{inj})^2)^2} + \frac{1}{2(x_p^2+(z_p-R-h_{inj})^2)^{\frac{3}{2}}} \right) \quad (20)$$

$$m_E = m_E^{ref} \sqrt{\frac{P_{excE}}{P_{ref}}} \quad (21)$$

$$\overline{E_Z} = \frac{1}{L_{CE}h} \int_{-L_{CE}/2}^{+L_{CE}/2} \int_{-h}^0 E_Z dz dx \quad (22)$$

$$\overline{E_Z} = m_E f_E^0 = \frac{m_E}{\pi h L_{CE}^2 \omega \epsilon_0} \left[ 2 \left( \frac{\sqrt{(L_{CE}/2)^2 + z_0^2}}{z_0} - \frac{\sqrt{(L_{CE}/2)^2 + z_1^2}}{z_1} \right) + \left( \frac{(L_{CE}/2)^2 + 2z_1^2}{z_1 \sqrt{(L_{CE}/2)^2 + z_1^2}} - \frac{(L_{CE}/2)^2 + 2z_0^2}{z_0 \sqrt{(L_{CE}/2)^2 + z_0^2}} \right) \right] \quad (23)$$

$$z_0 = -R - h_{inj} - h \quad z_1 = -R - h_{inj} \quad (24)$$

From the multiple partial image method and (23), the contributions of the reflections due to the ground plane and air-dielectric interface can be added together, as given by (26). The first term is the direct contribution of the dipole, the second term is due to the reflection to the ground plane, and the last two infinite sums are the contributions of the secondary images. As suggested in Part I of this paper, 5 to 8 secondary images are sufficient to converge at less than 1 % of the actual E-field value with typical PCB dimensions and scanning height. The authors use 20 images to guarantee the convergence. A simplification of (26) can be made to reduce the number of terms, as the first two terms are dominant for small values of  $R$ . Then, (26) can be simplified into (29). For  $R$  ranging between 1 and 10 mm,  $h$  ranging between 0.2 and 2 mm, and  $\epsilon_r$  between 2 and 5, the maximum relative error introduced by (29) reaches 8 %. The function  $f_{\bar{E}}$  is the average E-field along the line section for  $m_E$  equal to 1 A·m.

$$f_{\bar{E}} = K' f_E^0(z_0, z_1) + K' f_E^0(-z_0, -z_0 + h) + \sum_{n=1}^{\infty} [K'(-K)^n f_E^0(-z_0 + 2nh, -z_0 + 2(n+1)h)] + \sum_{n=1}^{\infty} [K'(-1)^{n+1} K^n f_E^0(z_0 - 2nh, -z_1 + 2nh)] \quad (26)$$

$$K = \frac{1-\epsilon_r}{1+\epsilon_r} \quad (27) \quad K' = 1 + K \quad (28)$$

$$f_{\bar{E}} = \frac{2}{1+\epsilon_r} \left( f_E^0(z_0, z_1) + f_E^0(-z_0, -z_0 + h) \right) \quad (29)$$

Substituting (26) or (29) into (19) leads to the maximum power  $P_{E_{max}}$  required during E near-field injection (30) to produce the same average field along  $L_{CE}$  as an incoming plane wave of amplitude  $E_{max}^{FF}$ . Using (30) to determine  $P_{E_{max}}$  also requires us to assume a likely value of  $L_{CE}$ , which may be based on a preliminary analysis of the possible sensitive traces or pins of the board under test.

$$P_{E_{max}} = \frac{P_{ref}}{1 + \left( \frac{f}{f_{CE}} \frac{\epsilon_r}{\epsilon_{eff}} \right)^2} \left( \frac{2E_{max}^{FF}}{m_E^{ref} f_{\bar{E}} \epsilon_r} \right)^2 \quad (30)$$

(30) is also based on the infinite large ground plane assumption. As in Section III.B, the relative difference between the average E-field computed with the finite and infinite ground planes is plotted vs. the scan height  $R$  for three different board sizes  $W_{board}$ , as shown in Fig 2-b. The result shows that the relative difference remains less than 5 %, as long as the scanning height is smaller than nearly one fifth of the board.

#### IV. CASE STUDY DESCRIPTION

##### A. Case Study 1 – Bandgap Reference

In the first case study, NFSI and RS estimation are done at the IC level. A micropower bandgap reference (LTC1798-2.5 from Analog Devices) is considered. It produces a 2.5 V reference voltage from a 5 V input voltage. The IC is mounted on a plastic SO8 package. The exact package encapsulation plastic material and its electrical permittivity are unknown. We assume that standard epoxy molding compound is used, with  $\epsilon_r$  ranging between 3.5 and 4. This circuit is mounted on a 10 cm × 10 cm four-layer board dedicated to TEM cell tests, with a complete ground plane on the top layer. The IC is isolated on the top layer, except short traces connected to the input and output pins, as shown in Fig. 4. The failure criterion is a deviation of +/- 10 mV of the output voltage.

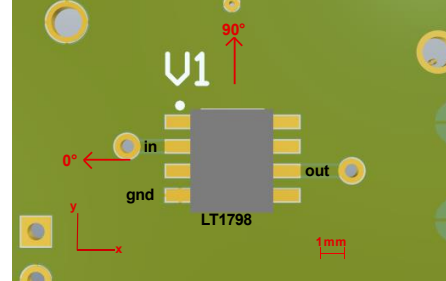


**Fig. 4.** Scan area and orientation of case study 1 (Bandgap reference)

##### B. Case Study 2 – Operational Amplifier

In the second case study, NFSI and RS tests are done at the PCB level. This case consists of an op-amp (LMV651 from Texas Instruments) in non-inverter amplifier configuration. The electrical diagram is shown in Fig. 5. The IC is supplied symmetrically between +/- 2.5 V. It is mounted on a 10 cm × 10 cm FR4 four-layer board dedicated to TEM cell tests, with a complete ground plane on internal layers. The IC, the external passive devices, and the PCB traces are placed on the top layer, as shown in Fig. 6. The non-inverting input (V+) is tied to the ground by an RC load through a 40 mm long line. The output voltage is measured by an oscilloscope through a 36 mm long line.

The conducted susceptibility of this op-amp has been studied in a previous study [14]. The circuit is sensitive to RF voltages coupled on both inverting (V-) and V+ inputs of the op-amp, which may lead to positive or negative offset on the output voltage. Up to 100 MHz, the main failure mechanism is related to the slew-rate limitation of the op-amp. It is dependent on the differential-mode (DM) voltage and always results in a positive failure. Above 100 MHz, the offset is mainly linked to a weak distortion due to the input differential pair of the op-amp. The

sign and the amount of EMI-induced offset depends on both common-mode (CM) and DM RF voltage amplitude and phase, according to a non-linear relationship. In this study, the failure criterion is set as a maximum deviation of +/- 10 mV of the output voltage.

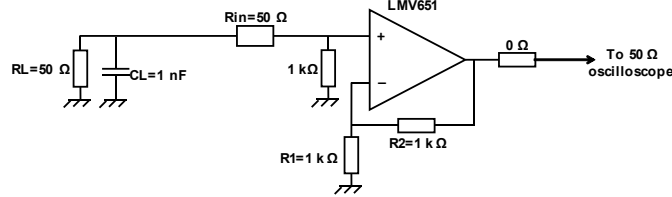


**Fig. 5.** Electrical diagram of case study 2 (op-amp board)

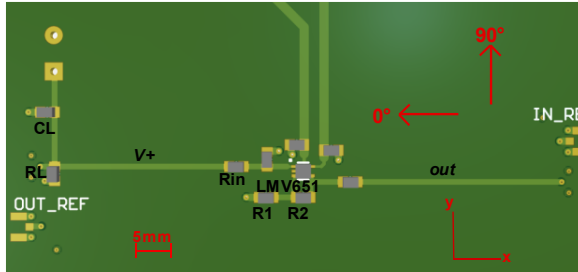


**Fig. 6.** Scan area and orientation of case study 2 (op-amp board)

### C. Experimental Set-up

The purpose of both case studies is to verify that the RS level measured when the device under test (DUT) is illuminated uniformly can be estimated from NFSI results. A convenient approach adapted to RS testing at the PCB and IC levels is the transverse electromagnetic and gigahertz transverse electromagnetic (TEM/GTEM) cell. Although the polarization of the TEM wave within the cell is fixed, the method is repeatable. The field amplitude within the cell is known with good precision and can reach several hundred V/m with an excitation of only a few watts. The board under test can be oriented to the GTEM input connector according to four directions: 0°, 90°, 180° and 270° according to the orientation of the DUT to the cell septum. RS tests are carried out with a GTEM cell model Schaffner GTEM250. 0° and 90° directions of the case studies in the GTEM cell are shown in Figs. 4 and 6. In 0° and 180° orientation, the H-field produced in the GTEM cell is oriented along the Y-axis, while it is oriented along the X-axis in 90° and 270° orientation.

The calibrated E and H-field injection probes described in Part I of this paper are reused. NFSI tests are done with three field components: Ez, which refers to the test with normal E-field probe made of a 4 mm long tip at the end of a semi-rigid coaxial cable, and Hx and Hy with the tangential H-field probe oriented along x and y directions consisting of a 5 mm diameter circular loop that terminates a semi-rigid coaxial cable. In both case studies, the scan altitude is set at 2 mm above the PCB surface. The scan altitude is chosen to place the injection probe as close as possible to the board under test, without any risk of contact with mounted components. The scan step is 2 mm along the X-axis and 1 mm along the Y-axis. NFSI and GTEM cell tests are done from 10 MHz to 3 GHz. Two power amplifiers are used for the range 10 MHz to 1 GHz and 1 to 3 GHz, with

power capability limited to 46 dBm and 44 dBm, respectively. During the GTEM cell tests, the maximum E-field is limited to 1,000 V/m and 800 V/m in each frequency range. The maximum power during the NFSI tests is limited to 40 dBm in order to avoid overheating of the injection probes.

## V. EXPERIMENTAL RESULTS

### A. Experimental Results of Case Study 1

#### 1) GTEM cell results

Fig. 7 presents the susceptibility levels of the bandgap reference measured in the GTEM cell. Results from 10 to 100 MHz are not shown as no failures were detected. Failures trigger between 200 MHz and 1.2 GHz, and around 1.7 GHz. Regardless of the frequency, the disturbance induces a negative offset voltage on the bandgap reference output. Depending on the orientation of the DUT in the GTEM cell, susceptibility peaks arise either around 300 MHz or 600 MHz. Some conclusions can be drawn about the nature of the coupling. The differences between the susceptibility levels measured in 0° and 90° (or 180° and 270°) orientations indicate that the H-field coupling contributes significantly. If only E-field couples, susceptibility levels will be similar regardless of the DUT orientation. However, E-field coupling also contributes to the observed failures because of the differences measured between the orientations 0° and 180° (or 90° and 270°).

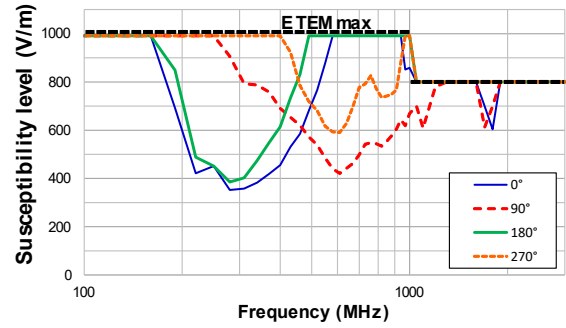


**Fig. 7.** Susceptibility level of the bandgap reference in the GTEM cell

#### 2) NFSI results

NFSI tests produce a massive amount of data that needs to be carefully analyzed to clarify the coupling mechanisms that lead to a failure. Only specific significant results are shown in this paper in order to clarify the coupling mechanisms. Figs. 9 to 11 present the susceptibility maps obtained with the three tested field components at three different frequencies. The positions of the susceptibility maxima change with the frequency. Fig. 8 shows the minimum probe excitation power required to induce a failure in the susceptibility maxima positions.

Irrespective of the frequency, a negative offset is generated on the DUT output. During Hy injection, the coupling is mainly located on the output pin up to 350 MHz, and then extends to the input pin. At 300 MHz, although the coupling is maximum when the H-field probe is placed above the die (Fig. 10 on the left), the coupling arises both on the input and output package leads and bonding wires. Because of the limited spatial resolution of the injection probe, simultaneous couplings arise

on both package interconnects and their contribution tends to add up. The contribution of individual coupling on each package interconnect cannot be separated. Above 500 MHz, the coupling is localized between the input and the ground pins. An interesting observation is that there is nearly no offset when the probe is placed in-between these pins. The RF voltages induced on both pins tend to counterbalance. Depending on the frequency, the coupling may appear mainly on the input or the ground pin (e.g. at 1 GHz). During Hx injection, the coupling area is localized above the y-oriented parts of the input and the ground pins within the IC package (package leads and bonding wires). However, contrary to Hy injection, no offset compensation is observed. During Ez injection, the coupling area is localized above the center of the IC package, regardless of the frequency. The coupling is certainly mainly concentrated on the die pad.

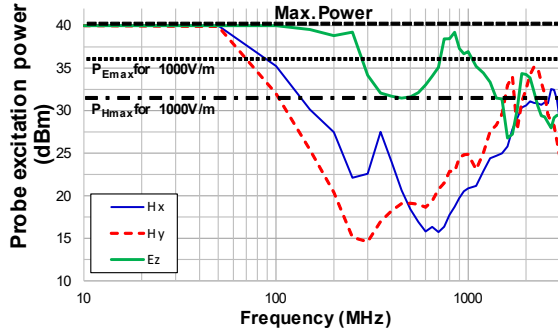


**Fig. 8.** Susceptibility level of the bandgap reference in NFSI tests

There are some correlations between GTEM cell and NFSI results. The susceptibility peak around 300 MHz in GTEM cell tests for the 0° and 180° directions is also visible in the Hy injection test. In the 0° and 180° orientations, only the Hy component is seen in the GTEM cell. Similarly, the susceptibility peak around 600 MHz in GTEM cell tests for 90° and 270° directions is also visible in the Hx injection test. The peak around 1.7 GHz appears both in GTEM cell and Ez injection results. However, the post-processing of NFSI results is required to verify the link between GTEM cell and NFSI results. Moreover, the direct comparison between the power excitation during E and H-field injection could be misleading as probe moments are different. The extent of E and H-field couplings cannot be determined without post-processing.

### 3) Radiated susceptibility estimation from NFSI results

The methodology described in Section II is used to estimate the RS level from NFSI results. It requires the identification of the minimum probe excitation power from NFSI maps, probe calibration data, and geometrical and electrical information concerning the DUT. However, the exact information about the internal geometry of the IC package and die is unknown in practice. The identification of coupling areas and geometry rely only on the NFSI maps and external dimensions of the IC package. For H-field, NFSI maps show that the coupling arises on package leads. As shown in [15] and [16], radiated coupling on IC package pins can be modeled similarly as for a two-conductor transmission line, formed by the package lead and

the ground plane below. The equivalent line structure is a microstrip line. As the Taylor model is considered in this study, only coupling on the horizontal parts of the package is considered. Only two geometrical parameters are required to compute the average field produced by the injection probe in the estimator (9): the coupling length, which is deduced from the NFSI maps, and the distance to the ground. According to the external dimensions of the package provided by the manufacturers which give the height of the lead frame, the package leads are assumed to be placed a constant height of 0.8 mm above the top layer of the PCB. Fig. 11 shows that the coupling of Ez arises above the die pad. As no internal details about the IC package are available, the following E-field coupling model is assumed: the die pad and the ground plane on the PCB top layer form a two-conductor line. The separation between both conductors is also supposed to be equal to 0.8 mm and the coupling length is extracted from the NFSI maps.

From NFSI maps, the sensitive pins are identified at each frequency and the coupling length is extracted according to the approach described in Section II.B. Depending if the field couples on the input and the ground pins, the coupling length is set to 4 mm for Ez, 3 or 6 mm for Hx, and 4 or 8 mm for Hy. The exact permittivity of the package is unknown so  $\epsilon_r$  and  $\epsilon_{eff}$  are assumed to be equal to 4. Finally, the contributions of couplings of the E and H-fields on different areas are added. This is a limitation of the proposed approach, since the phase of each coupling contribution cannot be measured in NFSI. If the incoming wave couples simultaneously on several pins or traces, and if the induced effects counterbalance, this effect cannot be measured accurately in NFSI since the injection is local. The risk is overestimation of the predicted RS. To prove the validity of the RS estimation method, the estimated RS level is compared with GTEM cell results. However, the H-field is oriented either along x or y directions in the GTEM cell, as explained in Section IV.C. Therefore, Hx and Hy NFSI results should not be combined. RS in 0° and 180° orientations is estimated from Ez and Hy NFSI results, whereas Ez and Hx NFSI results are used to estimate RS in 90° and 270° orientations.

Initially, (17) and (30) are used to determine the maximum probe excitation power to produce the same effect as a 1,000 V/m plane wave on the DUT. From the geometrical parameters of the board, the scan altitude, and the calibration parameters of the probes, the maximum power for E and H-field injections ( $P_{Emax}$  and  $P_{Hmax}$ ) are equal to 36 dBm and 32 dBm, respectively using a coupling length of 8 mm. These power limits are plotted on Fig. 8. Proving their validity by a direct comparison between GTEM and NFSI results is not straightforward, since E and H field coupling may coexist during GTEM cell test. These limits are relevant in a RS risk assessment only if a failure arises at least during one NFSI test below the power limit. This relevance is confirmed by the comparison between Figs. 7 and 8. As shown in Fig. 7, in GTEM cell, failures arise under less than 1000 V/m between 170 MHz and 1 GHz. Although failures arise in E-field injection below  $P_{Emax}$  only between 270 and 700 MHz, an excitation below  $P_{Hmax}$  is enough to induce failure during H-field injection between 100 MHz and 1 GHz. As no

failures are missed between 170 MHz and 1 GHz, the RS risk assessment from NFSI results is possible based on  $P_{E\max}$  and  $P_{H\max}$ . The lack of failure during E-field injection below  $P_{E\max}$  between 170 and 270 MHz and between 700 MHz and 1 GHz suggests that the DUT is not sensitive to E-field coupling on these frequency ranges.

A first validation step of the proposed estimator of RS

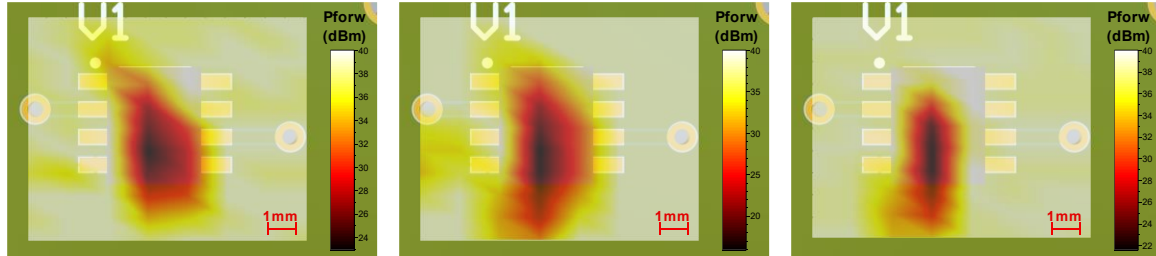


**Fig. 9.** Hx NFSI maps of the reference bandgap: 300 MHz (left), 600 MHz (center), 1 GHz (right)

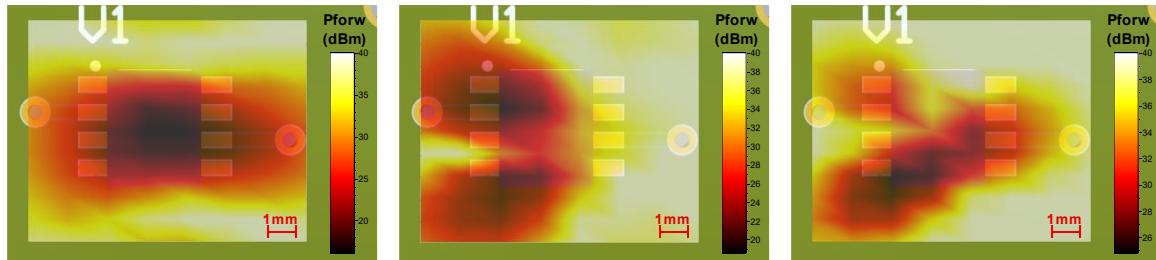


**Fig. 10.** Hy NFSI maps of the reference bandgap: 300 MHz (left), 600 MHz (center), 1 GHz (right)

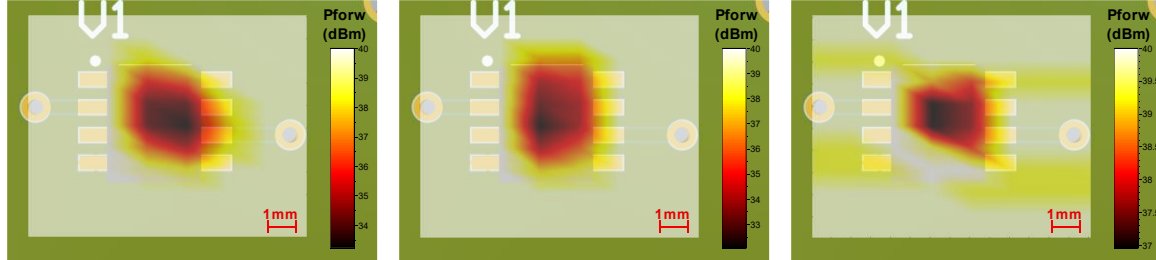


**Fig. 11.** Ez NFSI maps of the reference bandgap: 300 MHz (left), 600 MHz (center), 1 GHz (right)

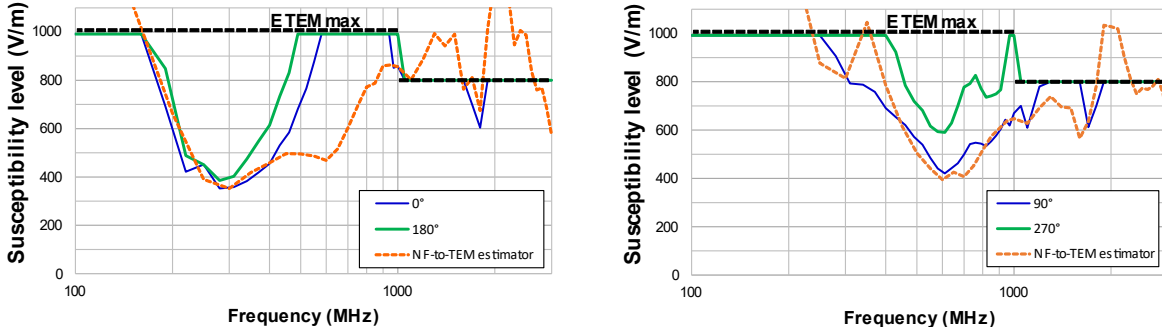


**Fig. 12.** Comparison between susceptibility level measured in the GTEM cell and the NFSI-based susceptibility estimator: for 0°/180° orientation (left), 90°/270° orientation (right)

Up to 350 MHz, the coupling is essentially magnetic ( $Z_N$  exceeds 2) and becomes electric between 1.5 and 2.7 GHz ( $Z_N$  is less than 0.5). Relatively good correlation between the GTEM cell for 0° orientation and the NFSI-based estimator is observed up to 400 MHz. For the 0° orientation, E and H-field contribution tends to add up, contrary to the 180° orientation. However, NFSI-based estimation tends to overestimate the RS

consists in combining Ez and Hy injection results according to (9) to estimate the RS level for the 0 and 180° orientations, as only Hy couples to the DUT in the GTEM cell. Similarly, as only Hx couples for the 90° and 270° orientations, Ez and Hy injection results are combined to estimate the worst-case RS level in these orientations. Results are presented in Fig. 12.

level between 400 and 950 MHz. This can be explained by the simultaneous coupling of H-field on the input and ground pins during the GTEM cell test, which tends to counterbalance. This effect is illustrated in Figure 13, which shows a simplified geometrical description of the package pins. In 0° and 180°, the H-field in the GTEM cell is oriented along the Y-axis and couples on the X-oriented part of the pins. Due to the orientation

of the electromotive forces induced on both pins, the RF voltage generated between the input and the ground pins tends to be attenuated. This type of effect does not appear for the 90° and 270° orientation as the H-field in the GTEM cell is oriented along the X-axis. The effect of the electromotive force induced on input and ground pins tends to add up and increase the RF voltage generated between the input and the ground pins. In 90° and 270°, good agreement between GTEM cell results and the NFSI-based estimator is obtained between 400 and 1100 MHz. The susceptibility peak at 1.7 GHz is also predicted by the NFSI-based estimator with the correct order of disturbance level. The NFSI-based estimator tends to overestimate the RS level in GTEM between 1.1 and 1.6 GHz, and above 2.4 GHz. An offset tends to appear in this frequency range during the GTEM cell test, but the power limit of the amplifier is reached. This difference may be explained by compensation between E and H-field coupling in the GTEM cell. For the same reason, the proposed method underestimates the RS level in the 90° and 270° orientations between 300 and 400 MHz. The cumulative effect of the simultaneous couplings of E and H fields on several IC pins is not correctly determined from NFSI maps.

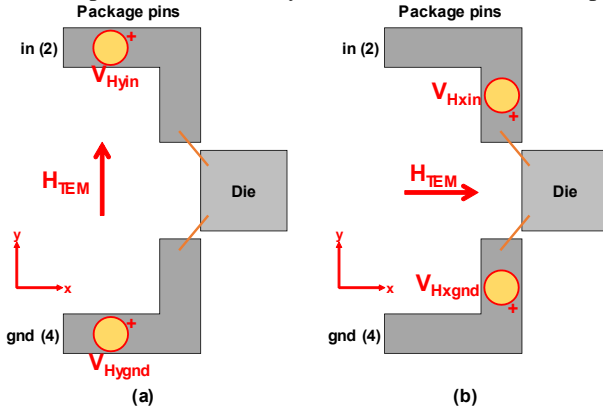


**Fig. 13.** Effect of board orientation in the GTEM cell on H-field coupling: (a) 0° and 180° orientation, (b) 90° and 270° orientation

Secondly, a worst-case estimation of the RS level is made by considering the minimum value between the two previous NFSI-based estimators. This worst-case estimator is compared with the minimum RS level in the GTEM cell, regardless of the orientation, as shown in Fig. 14. Relatively good correlation is observed between 150 and 1500 MHz, where the maximum difference does not exceed 100 V/m. The estimator also correctly predicts the lack of failures below 150 MHz and between 1.9 and 2.5 GHz. Differences can be explained by uncertainty about the permittivity and the internal geometry of the IC package, but also by the differences between NFSI and TEM cell set-ups. They can also be explained by the compensation between E and H-field coupling during GTEM cell tests. However, this result shows that, even though compensation effects arise due to simultaneous coupling on several pins, this does not exist for all incoming wave orientations. As a result, the proposed NFSI-based estimator can determine the worst-case situations without excessive overestimation.

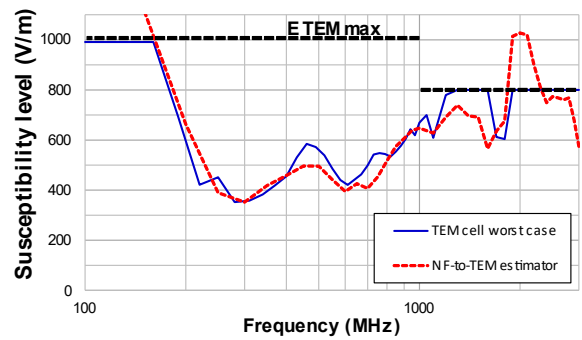


**Fig. 14.** Comparison between worst-case susceptibility levels measured in the GTEM cell and NFSI-based susceptibility estimator

## B. Experimental Results of Case Study 2

### 1) GTEM cell results

Fig. 15 presents the susceptibility levels of the op-amp board measured in the GTEM cell. Depending on the frequency and board orientation, failures are related to positive or negative offset. Except around 100 MHz for the 0° orientation, the main susceptibility peak is around 700 and 800 MHz, regardless of the board orientation.

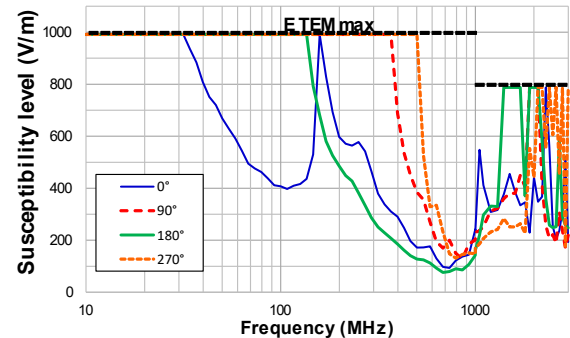


**Fig. 15.** Susceptibility level of the op-amp in the GTEM cell

Above 1 GHz, the susceptibility level tends to vary abruptly with frequency and board orientation, with numerous changes of the offset sign. This effect can be explained by the long electrical dimensions of the board above 1 GHz and its relative complex geometry, that leads to a complex relationship between the CM and DM RF voltages applied on the op-amp inputs. Up to 1 GHz, susceptibility is larger in 0° and 180°, where the V- input and output traces are parallel to the GTEM septum which optimizes H-field coupling, contrary to the 90° and 270° orientations. The measurement differences between the four orientations reveals that both E and H-field couplings contribute to failure generation.

### 2) NFSI results

Figs. 16, 17 and 18 present the susceptibility maps obtained for Hx, Hy and Ez components at two different frequencies. The positions of the susceptibility maxima change with the frequency. Fig. 19 shows the minimum probe excitation power required to induce a failure in the susceptibility maxima positions.

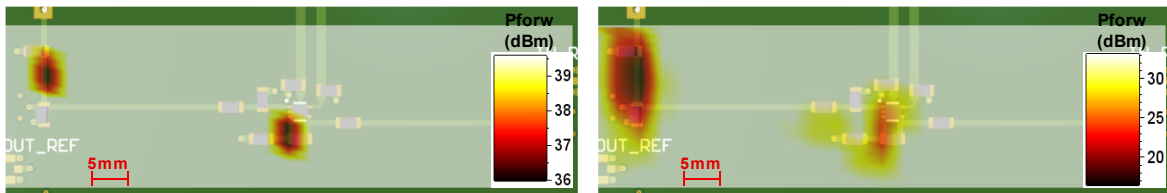


**Fig. 16.** Hx NFSI maps of the op-amp board: 200 MHz (left), 1000 MHz (right)

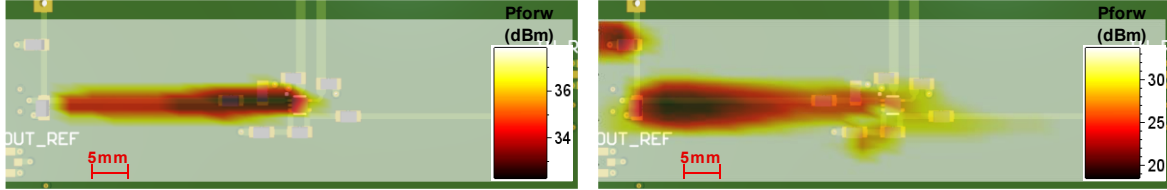


**Fig. 17.** Hy NFSI maps of the op-amp board: 200 MHz (left), 1000 MHz (right)

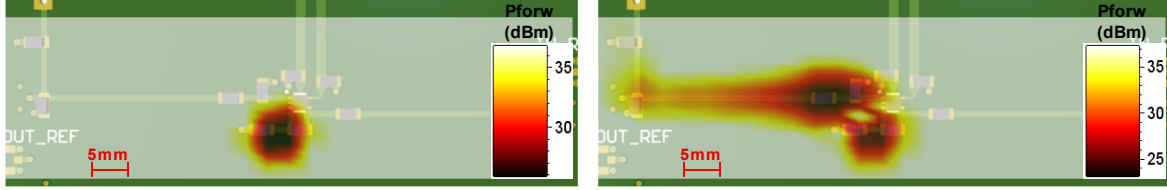


**Fig. 18.** Ez NFSI maps of the op-amp board: 200 MHz (left), 1000 MHz (right)

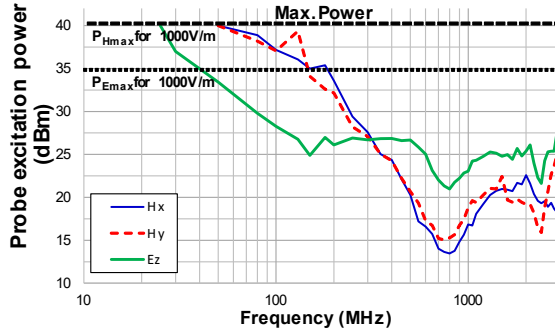


**Fig. 19.** Susceptibility level of the op-amp board in NFSI tests

During H-field injection, the coupling is mainly visible on the V+ input trace and leads to a negative offset, except below 180 MHz. In low frequency, H-field coupling is also seen on the output and feedback traces, resulting in a positive offset. At higher frequencies, for Hy injection, some coupling is also found on the V- input trace (around 1 and 3 GHz). For Hx injection, coupling is mainly done on the V- input trace and leads to a positive offset. During E-field injection, coupling appears on the V- input up to 550 MHz and leads to positive offset. Then, E-field coupling appears mainly on the V+ input between 600 and 900 MHz. At higher frequencies, E-field coupling arises on both op-amp inputs, resulting in changes of the offset signs with frequency. This complex behavior confirms the influence of the couplings of E and H-fields on op-amp inputs, which has an influence on the offset sign. This clarifies the strong variability of the RS in GTEM, according to the frequency and board orientation. NFSI results show that several coupling areas exist on the board, which may capture either E or H-field and lead to positive or negative offset. During a global illumination by a plane wave, the resulting effect on the offset varies strongly depending on how these different coupling contributions are combined on V+ and V-. There are also some correlations between GTEM cell and NFSI

results. The susceptibility peak around 700 MHz in the GTEM cell is also visible in E and H-field injection. However, the link between NFSI and GTEM cell results is not obvious and post-processing of NFSI results is required.

### 3) Radiated susceptibility estimation from NFSI results

The RS estimation methodology previously applied is reused. In this case study, the coupling arises mainly on PCB traces. Due to the small size of the IC package, its influence on coupling is disregarded. The height of the traces to the reference ground plane is 0.42 mm and the board  $\epsilon_r$  is set to 4.5. From NFSI maps, the sensitive traces are identified at each frequency. As the exact dimensions of PCB traces are known exactly, the coupling lengths are based on the dimensions of the identified sensitive traces. Depending if the field couples on the input, feedback and output traces, the coupling length is set to 8 or 16 mm for Ez, 8 or 11 mm for Hx, and 40 mm for Hy. Similar to the first case study, the contributions of couplings of E and H-fields are added, since the measurement of the phase of the induced RF voltage due to E and H-field coupling at trace ends is difficult in a real application board. Moreover, Ez NFSI results are combined either with Hx or Hy NFSI results, depending on the orientation of the board in the GTEM cell.

Initially, (17) and (30) are used to evaluate the maximum probe excitation power to produce the same effect as a 1,000 V/m plane wave on the DUT. From the geometrical parameters of the board, the scan altitude and the calibration parameters of the probes, the maximum power for E and H-field injection are  $P_{Emax} = 35$  dBm ( $L_{CE} = 8$  mm) and  $P_{Hmax} = 40$  dBm ( $L_{CH} = 40$  mm), respectively. As shown in Fig. 15, in GTEM cell, failures arise under less than 1000 V/m between 34 MHz and 1 GHz. In Fig. 19, failures arise in E-field injection below  $P_{Emax}$  between 40 MHz and 3 GHz, and in H-field injection below  $P_{Hmax}$  between 50 MHz and 3 GHz. Except between 34 and 40 MHz, no failures are missed during NFSI tests with the selected  $P_{Emax}$  and  $P_{Hmax}$  and RS risk assessment is possible. The discrepancy

between 34 and 40 MHz can be explained by the guess of coupling length in ((17) and (30), which remains unknown before the NFSI tests. In practice, an additional margin is recommended to compensate the uncertainty about the coupling length on the estimation of  $P_{E\max}$  and  $P_{H\max}$ .

A first validation step of the proposed estimator of RS consists in combining Ez and Hy injection results according to (9) to estimate the RS level for the  $0^\circ$  and  $180^\circ$  orientations. Similarly, as only Hx couples for the  $90^\circ$  and  $270^\circ$  orientations, Ez and Hx injection results are combined to estimate the worst-case RS level in both orientations. Results are presented in Fig. 20. Relatively good correlation between the GTEM cell for the  $180^\circ$  orientation and the NFSI-based estimator is observed between 180 MHz and 1 GHz. E and H-field contribution tends to add up, contrary to the  $0^\circ$  orientation.

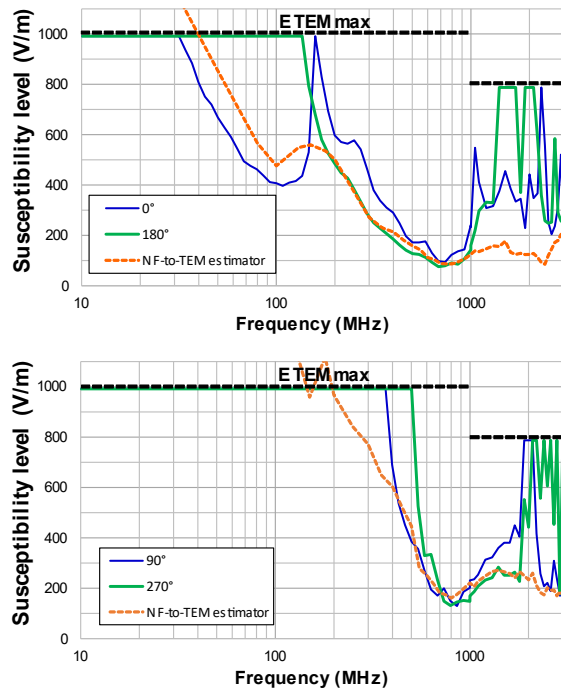


**Fig. 20.** Comparison between susceptibility levels measured in the GTEM cell and NFSI-based susceptibility estimator: for the  $0^\circ/180^\circ$  orientation (top), and  $90^\circ/270^\circ$  orientation (bottom)

However, above 1 GHz, the NFSI-based estimation overestimates the RS level, due to the simultaneous coupling of E and H-field on V+ and V-, which tends to counterbalance the induced offset. Similarly, NFSI-based estimation tends to underestimate the RS level below 150 MHz. In this range, the simultaneous coupling on V+ and V- during GTEM cell testing adds up to generate a positive offset. This cumulative effect cannot be produced during NFSI due to local coupling. Nevertheless, underestimation does not exceed 25 % of the actual RS level, and the susceptibility peak around 100 MHz is correctly predicted. Although this peak is not clearly visible on NFSI results (Fig. 19), NFSI post-processing reveals this effect because the H-field couples to both V+, V- and output traces around 100 MHz, while it couples only on V+ above 180 MHz. The widening of the coupling length reduces the required field to induce a failure. The same conclusions can be drawn from

the comparison between GTEM results in  $90^\circ$  and  $270^\circ$  and the NFSI-based estimator. Above 400 MHz, the post-processing of NFSI results provides an acceptable estimation of the RS level. Below 400 MHz, the proposed estimator tends to overestimate the susceptibility level because of the simultaneous coupling on V+ and V-. Nevertheless, the estimator predicts a high immunity level below 400 MHz for the  $90^\circ$  and  $270^\circ$  orientations, which is verified by GTEM cell measurement.

Second, as in the first case study, a worst-case estimation of the RS level is made by considering the minimum value between the two previous NFSI-based estimators, and is compared with the minimum RS level in the GTEM cell. As shown in Fig. 21, relatively good correlation is observed between 180 MHz and 1 GHz. The differences below 180 MHz and above 1 GHz are mainly due to simultaneous coupling on several PCB traces during GTEM cell testing. However, underestimation of the RS level does not exceed 25 % of the actual RS level, and the proposed NFSI post-processing provides the correct RS level estimate. It may be sufficient to assess the RS risks at the PCB level at the end of NFSI investigation.

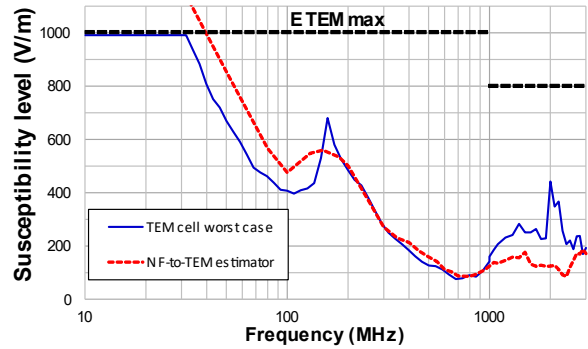


**Fig. 21.** Comparison between worst-case susceptibility levels measured in the GTEM cell and NFSI-based susceptibility estimator

## VI. CONCLUSION

The second part of this two-part paper has presented an estimator of the radiated susceptibility of a circuit or a PCB from NFSI results. The proposed post-processing method of NFSI results has been applied to two practical studies. In spite of the presence of non-linear devices and the simultaneous couplings on several traces or IC pins, the method provides a correct estimate of the worst-case radiated susceptibility level, at least up to 3 GHz. When simultaneous couplings arise, the precision of the estimator degrades, but it remains acceptable for susceptibility risk assessment purposes, since the estimated susceptibility level is determined correctly, and susceptibility peaks are detected. With this type of tool, a PCB designer can evaluate at the end of a preliminary NFSI campaign whether the PCB will introduce excessive non-compliance risk during susceptibility testing, or whether design improvements are required.

The problem of the simultaneous coupling is an intrinsic issue of any estimation method of the radiated susceptibility from NFSI results, since it is related to a fundamental difference

between far-field illumination and local near-field injection. Without any measurements or models of the different contributions of the incoming field coupling, determining how they should be combined is not straightforward. It constitutes one limitation of the proposed approach. Further research is required to find a method to determine from NFSI results how the different contributions of simultaneous radiated couplings actually combine. It is of major importance to improve the accuracy of the radiated susceptibility estimation for more complex PCB design with multiple traces connected to the same sensitive IC pins.

One advantage of NFSI in this risk assessment process is the reduced amount of excitation power compared to other radiated susceptibility tests, such as the Absorber-Lined Shield Enclosure or TEM cell. The NFSI user can make use of the formulations proposed in this paper to evaluate the amount of excitation power according to the calibration results of the injection probe and basic geometrical information of the DUT. One drawback of the proposed approach is that it is limited to investigation at the board or circuit level. The impact of cables or enclosures, which have a major impact on radiated susceptibility of electronic equipment, has not been considered in this study. These issues should be investigated in future studies.

## REFERENCES

- [1] IEC TS 62132-9, Integrated circuits – Measurement of electromagnetic immunity – Part 9: Measurement of radiated immunity – Surface scan method, International Electrotechnical Commission, 2014.
- [2] A. Boyer, E. Sicard, S. Bendhia, "Characterization of the Electromagnetic Susceptibility of Integrated Circuits using a Near Field Scan", *Elec. Letters*, vol. 43, No 1, pp. 15-16, 4th Jan. 2007, 10.1049/el:20073130.
- [3] N. Lacrampe, S. Serpaud, A. Boyer, S. Tran, "Radiated Susceptibility Investigation of Electronic Board from Near Field Scan Method", in *Proc. EMC Compo 2017*, Saint Petersburg, Russia, Jul. 2017, pp. 125-130.
- [4] A. Alaelidine, T. Ordas, R. Perdriau, P. Maurine, M. Ramdani, L. Torres, M. Drissi, "Assessment of the Immunity of Unshielded Multicore Integrated Circuits to Near Field Injection", in *Proc. Int. Zurich Symp. on EMC*, Zurich, Switzerland, Jan. 2009, pp. 361-364.
- [5] A. Boyer, S. Bendhia, E. Sicard, "Modelling of a Mixed-Signal Processor Susceptibility to Near-Field Aggression", in *Proc. 2007 IEEE Int. Symp. on EMC*, Hawaii, USA, Jul. 2007.
- [6] T. Dubois, J. J. Laurin, J. Raoult, S. Jarrix, "Effect of Low and High-Power Continuous Wave Electromagnetic Interference on a Microwave Oscillator System: From VCO to PLL to QPSK Receiver", *IEEE Trans. on EMC*, vol. 56, no. 2, pp. 286-293, Apr. 2014, 10.1109/TEMC.2013.2280670.
- [7] O. Kröning, M. Krause, M. Leone, "Near Field-Immunity Scan on Printed Circuit Board Level", in *Proc. 2010 IEEE 14th Workshop on Signal Propagation on Interconnects (SPI)*, May 2010, pp. 101-102.
- [8] K. Wang, D. Pommernike, J. M. Zhang, R. Chundru, "The PCB level ESD immunity study by using 3 Dimension ESD Scan System", in *Proc. 2004 Int. Symp. on EMC*, Aug. 2004, pp. 343-348.
- [9] A. Durier, S. Ben Dhia, T. Dubois, "Comparison of Voltages Induced in an Electronic Equipment during Far Field and Near Field Normative Radiated Immunity Tests", in *Proc. of 2019 Int. Symp. On EMC - EMC Europe 2019*, Barcelona, Spain, Sep. 2019.
- [10] A. Boyer, "A Rigorous Method to extrapolate Radiated Susceptibility from Near-Field Scan Immunity", in *Proc. 2019 Int. Symp. on EMC - EMC Europe 2019*, Barcelona, Spain, Sep. 2019.
- [11] D. Pommernike, G. Muchaidze, J. Koo, Q. Cai, J. Min, "Application and Limits of IC and PCB scanning methods for immunity analysis", in *Proc. 18th Int. Zurich Symposium on EMC*, Munich, Germany, Sept. 2007, pp. 83-86.
- [12] Altair FEKO, Electromagnetic Simulation Software, more information on [www.altairengineering.fr/feko](http://www.altairengineering.fr/feko)
- [13] P. Silvester, "TEM wave properties of microstrip transmission lines", in *Proc. Inst. Elec. Eng.*, vol. 115, no. 1, pp. 43–48, Jan. 1968.
- [14] A. Boyer, E. Sicard, "A Case Study to apprehend RF Susceptibility of Operational Amplifiers", 12th International Workshop on the Electromagnetic Compatibility of Integrated Circuits (EMC Compo 2019), Hangzhou, China, Oct. 21-23 2019.
- [15] A. Boyer, S. Ben Dhia, E. Sicard, "Modelling of a Mixed-Signal Processor Susceptibility to Near-Field Aggression", *2007 IEEE Symp. on EMC*, Honolulu, HI, USA, 9 – 13 July 2007, 10.1109/ISEMC.2007.209.
- [16] A. Boyer, B. Vrignon, M. Cavarroc, "Modeling Magnetic Near-Field Injection at Silicon Die Level", *IEEE Trans. on EMC*, vol. 58, no 1, Feb. 2016, pp. 257-268, 10.1109/TEMC.2015.2486041.



**A. Boyer** obtained a Masters degree in electrical engineering in 2004 and a PhD in Electronics from the French National Institute of Applied Sciences (INSA) in Toulouse, France, in 2007. He is currently an Associate Professor in the Department of Electrical and Computer Engineering at INSA, Toulouse. He carries out research at the Laboratory of Analysis and Architecture of Systems (LAAS-CNRS), as part of the 'Energy and Embedded Systems' research group.

His current research interests include EMC measurements, IC EMC and reliability modeling, and computer aided design (CAD) tool development for EMC (IC-EMC freeware).



**N. Nohier** received a doctorate in electronics from the French National Institute of Applied Sciences (INSA), Toulouse, in 1992. He is Professor at the University Paul Sabatier, Toulouse, and works at the Laboratory of Analysis and Architecture of Systems (LAAS-CNRS). First motivated by the control and modeling of rapid heat treatment, his interests shifted to the design and simulation of Power Devices. In 1996, he initiated the study of ESD protections using 2D electrothermal simulations at LAAS and studied TLP experiments. He has supervised more than 15 PhDs in ESD protection strategy (device and system level). Since 2016, he has focused on the reliability of space nanosystems. In 2019, he became director of the Toulouse University Space Center (CSUT).



**F. Caignet** received an MS degree in electrical engineering from the University of Toulouse, Toulouse, France, in 1995, and a PhD degree from the French National Institute of Applied Sciences (INSA), Toulouse, in 1999. From 1995 to 2000, he worked on signal integrity and EMC at the chip level at INSA. In 2001, he joined the Laboratory of Analysis and Architecture of Systems (LAAS), Toulouse, to work on the integration of optical links and devices into silicon chips, tackling challenges like propagation time on high complex architectures, EMC aspects, and cost. In 2006, he joined the electrostatic discharge (ESD) team of LAAS to work on ESD at a system level. His current research interests include developing measurement and simulation methodology to predict ESD impact at the IC level.



**S. Ben Dhia** obtained her Masters degree in electrical engineering in 1995, and a PhD in Electronic Design from the French National Institute of Applied Sciences (INSA), Toulouse, France, in 1998. Full professor at INSA-Toulouse (French engineering institute), Department of Electrical and Computer Engineering, she teaches digital electronics, IC testability and reliability, and analog and RF CMOS design. CEO of INSA Euro-Méditerranée, Fès, Morocco (2014-2017), she was responsible for the overall leadership and management of this new engineering institute. Her research interests at LAAS – CNRS Toulouse include signal integrity in nano-scale CMOS ICs, electromagnetic compatibility and reliability of ICs. She has authored or co-authored 3 books, more than 120

publications in peer-reviewed journals and conference proceedings, and supervised 14 PhD theses and 9 MSc theses.